

Boron-Functionalized Organic Framework as a High-Performance Metal-Free Catalyst for N₂ Fixation

Wenyang Zhou, Haoming Shen, Huanhuan Xie, Yiheng Shen, Wei Kang, Qian Wang,*
Yoshiyuki Kawazoe, and Puru Jena*



Cite This: *J. Phys. Chem. Lett.* 2021, 12, 12142–12149



Read Online

ACCESS |



Metrics & More

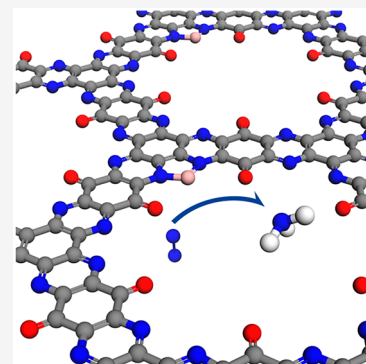


Article Recommendations



Supporting Information

ABSTRACT: Inspired by the recently synthesized covalent organic framework (COF) containing triquinoxalinylene and benzoquinone units (TQBQ) in the skeleton, we study the stability and properties of its two-dimensional analogue, TQBQCOF, and examine its potential for the synthesis of ammonia using first-principles calculations. We show that the TQBQCOF sheet is mechanically, dynamically, and thermally stable up to 1200 K. It is a semiconductor with a direct band gap of 2.70 eV. We further investigate the electrocatalytic reduction of N₂ to NH₃ on the Boron-functionalized TQBQCOF sheet (B/TQBQCOF). The rate-determining step of the catalytic pathways is found to be *N–N → *N–NH for the distal, alternating, and enzymatic catalytic mechanisms, with the corresponding overpotentials of 0.65, 0.65, and 0.07 V, respectively. The value of 0.07 V is the lowest required voltage among all of the N₂ reduction catalysts reported so far, showing the potential of B/TQBQCOF as a metal-free catalyst to effectively reduce N₂ to NH₃.



Nitrogen is an indispensable element in all life forms on Earth^{1,2} and makes up 78% of the volume of its air. The bond energy of N₂ is 940.95 kJ/mol. Hence, under mild reaction conditions, it is difficult to break its inert N≡N triple bond and further reduce it into ammonia (NH₃).^{3,4} As an important source of artificial fertilizer, NH₃ is also a carbon-free hydrogen energy carrier. To date, in addition to the natural biological N₂ fixation based on nitrogenase enzymes, the synthesis of NH₃ in industry mainly relies on the Haber–Bosch process, which requires harsh reaction conditions, consuming about 1.4% global energy annually.^{5,6} In addition, the raw material H₂ is necessary, which consumes a large number of nonrenewable resources and leads to excessive CO₂ emissions with serious impact on the environment.^{7,8} Electrolytic N₂ reduction reaction (NRR) under mild conditions is considered as a low-cost and environmentally friendly process for NH₃ synthesis.^{7,9–11} In this process, high-efficiency catalysts can increase the rate and selectivity of the overall catalytic reaction and reduce energy consumption.¹² Hence, the electrochemical NRR, driven by renewable energy where raw materials are N₂ and H₂O, is a viable alternative to the energy-consuming Haber–Bosch process.¹³

Most of the traditional catalysts for NRR reported so far are based on noble metals such as Ru,¹⁴ Rh,¹⁵ Pd,¹⁶ Au,¹⁷ and Pt;¹⁸ transition metals (TMs) such as Ti,¹⁹ V,²⁰ Cr,²¹ Mn,²² Fe,²³ Co,²⁴ Ni,²⁵ Nb,²⁶ Mo,²⁷ and W;²⁸ and p-block metals such as Bi^{29,30} and Sn;^{31,32} and their compounds. However, the scarcity of noble metals, and the limited NH₃ yield Faraday efficiency of transition metals along with their environmental pollutions hinder their widespread industrial application. On

the contrary, non-metal catalysts have inherent advantages of low cost and environmental friendliness, and exhibit excellent activity and long-term durability with less poisoning and crossover effects.^{33–37} Therefore, the development of non-metal catalysts for NRR has great economic value and scientific significance, and has been hotly pursued in recent years. In this context, the recently synthesized honeycomb-like covalent organic framework with triquinoxalinylene and benzoquinone units, TQBQ-COF,³⁶ could be a potential candidate, because it has a unique geometry with large regular pores that can offer enough space to accommodate intermediates. In particular, introduction of the electron-deficient boron (B) atom into TQBQCOF may be beneficial to design a metal-free catalyst for NRR. The potential of B atom for nitrogen fixation in metal-free catalysts has been demonstrated as it can further reduce N₂ molecule to B₂N₂ or [B₂N₂]²⁻ due to the weak Lewis base feature of N₂ molecules.² In addition, similar to TM-based catalysts where the high performance mainly stems from the combination of the empty and occupied d orbitals, sp³ hybridized B atoms also possess occupied and empty orbitals; the empty orbitals can accept the lone pair of electrons from N₂ and the occupied orbitals can back-donate electrons to the antibonding orbitals of N₂ to weaken its N≡N

Received: August 1, 2021

Accepted: November 19, 2021

Published: December 16, 2021



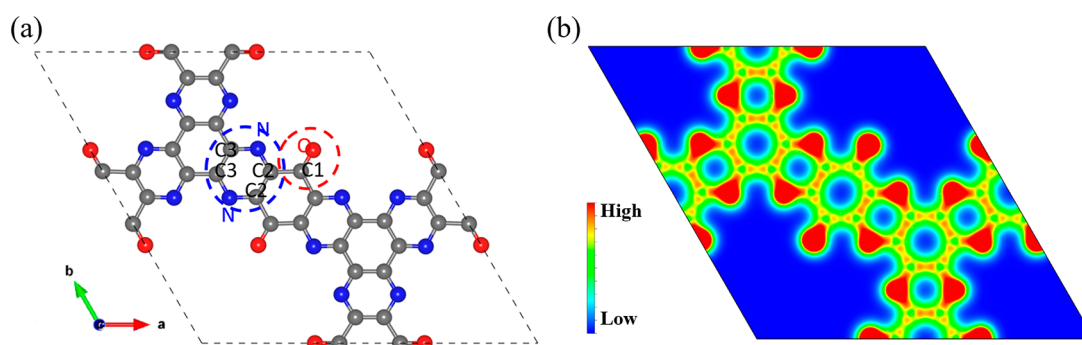


Figure 1. (a) Optimized structure and (b) electronic charge density of the TQBQCOF sheet. C, N, and O atoms are labeled by gray, blue, and pink spheres, respectively.

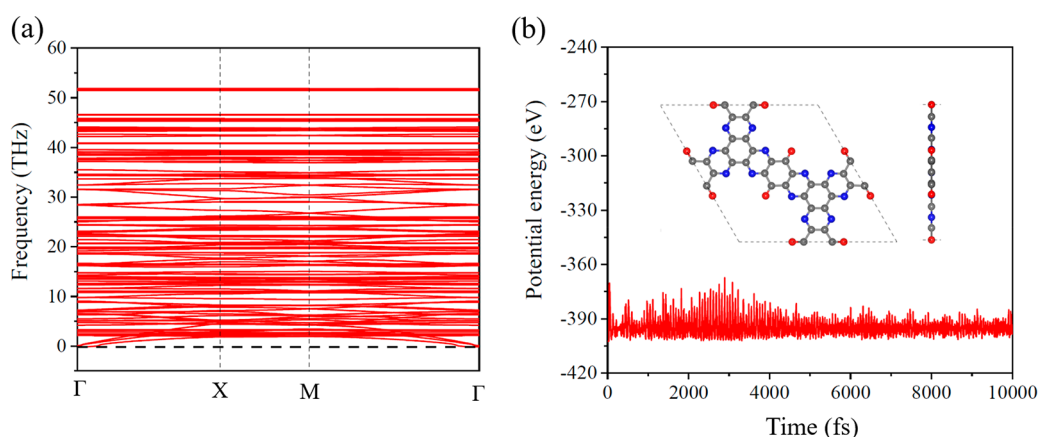


Figure 2. (a) Phonon spectrum and (b) total potential energy fluctuation of TQBQCOF during AIMD simulation at 1200 K.

bond. Therefore, it is possible to achieve a superior metal-free catalyst for reduction of N_2 to NH_3 by introducing the sp^3 hybridized B atoms to a stable TQBQCOF material.

In this work, we study the geometric and electronic structure as well as the mechanical properties of a 2D sheet, TQBQCOF, which can be chemically exfoliated from the recently synthesized covalent organic framework.³⁶ In addition, we use it as a substrate for metal-free catalyst for N_2 catalytic reduction. We show that, unlike traditional 2D materials such as graphene that requires structural defects to anchor metal or B atoms, the TQBQCOF sheet contains many active sites for anchoring B, making it unnecessary to introduce any artificial structural defects. We show that the B-functionalized TQBQCOF sheet can act as a promising metal-free catalyst for effective reduction of N_2 to NH_3 .

Our calculations are based on the density functional theory (DFT), using the projector augmented wave (PAW) potential³⁸ as implemented in the Vienna ab initio simulation package (VASP).³⁹ To describe the interactions of electrons, we adopt the Perdew–Burke–Ernzerhof (PBE)⁴⁰ exchange–correction functional within the generalized gradient approximation (GGA). A kinetic energy cutoff of 520 eV and a $3 \times 3 \times 1$ Monkhorst–Pack⁴¹ mesh are used for electronic structure and geometry optimization. The accuracy of our results is verified by increasing the K -point mesh to $4 \times 4 \times 1$. The convergence criteria of total energy and force components are set as 0.0001 and 0.01 eV/Å, respectively. A vacuum space of 16 Å along the z -direction is added to avoid layer interactions. Details on the binding energy and calculations of free energy

diagrams can be found in Section S1 of the Supporting Information (SI).

The 2D TQBQCOF sheet is exfoliated from the synthesized AB stacked covalent organic frameworks (COFs) with triquinoxalinyne and benzoquinone units (TQBQ) in its skeleton. The distance between the two layers is 3.07 Å,³⁶ which is comparable to that of some van der Waals crystals, including graphite (3.35 Å)⁴² and h-BN (3.33 Å).^{43,44} Its unit cell, shown in Figure 1a, consists of multiple carbonyls and pyrazine groups and contains 48 atoms with 30 carbon (C), 12 nitrogen (N), and 6 oxygen (O) atoms. The optimized geometry is a hexagonal planar structure with the lattice group symmetry of $P4/mbm$ (D4h5). The optimized lattice parameters of the unit cell are $a = b = 16.70$ Å and $\gamma = 120^\circ$. In this structure, the O and N atoms are equivalent, while there are three different types of C atoms, including C1 in carbonyls (C=O), and C2 and C3 in pyrazines, as marked in Figure 1a. The Wyckoff positions of the C, N, and O atoms in TQBQCOF are shown in Table S1 of the SI. Also, its structural data (POSCAR) can be found in SI Section S3. The specific bond lengths and angles are calculated and listed in Table S2 in the SI. The charge density in the TQBQCOF is mainly distributed on the N and O atoms as illustrated in Figure 1b.

Before the study of its electrocatalytic properties, we first calculate the phonon dispersion of TQBQCOF with a $2 \times 2 \times 1$ supercell to examine the dynamic stability of TQBQCOF as shown in Figure 2a; no imaginary modes are found in the entire first Brillouin zone, confirming the dynamical stability of TQBQCOF. We then perform ab initio molecular dynamics

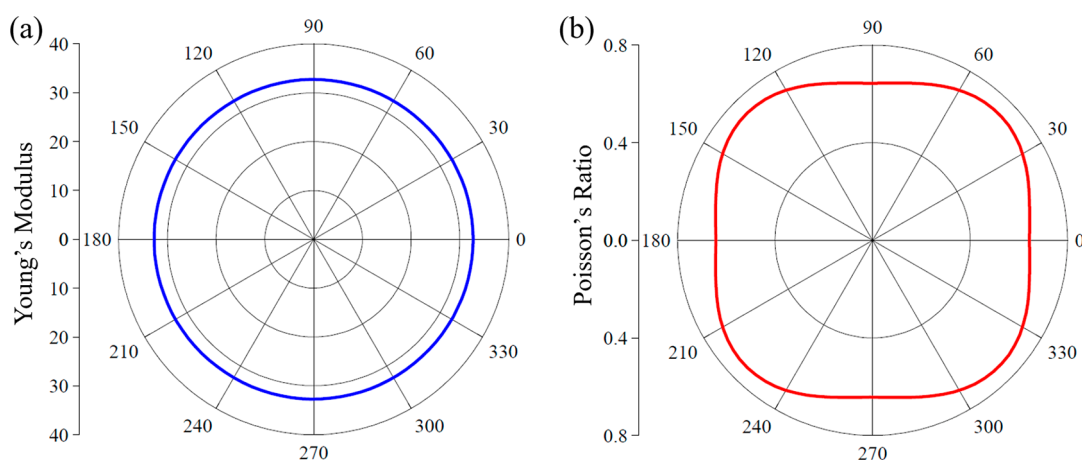


Figure 3. Polar diagrams of (a) $Y(\theta)$ and (b) $\nu(\theta)$ of TQBQCOF.

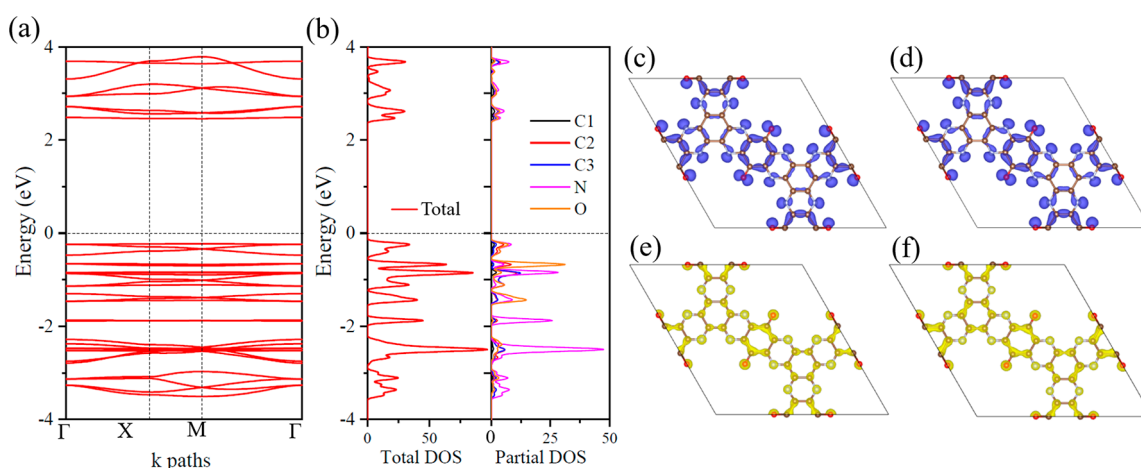


Figure 4. (a) Electronic band structure and (b) corresponding TDOS and PDOS, band decomposed charge density distributions of the (c) second highest occupied band, (d) highest occupied band, (e) lowest unoccupied band, and (f) second lowest unoccupied band of TQBQCOF. The isosurface value is $0.003 \text{ e}/\text{\AA}^3$.

(AIMD) simulations from 300 to 900 K using the Nosé thermostat⁴⁵ to study its thermal stability. Figure 2b depicts the change of the total energy with respect to time and the final configuration of TQBQCOF after 10 ps AIMD simulation at 1200 K. One can see that the energy fluctuates at a constant value, and all bonds remain intact, confirming that TQBQCOF can withstand the high temperature of 1200 K.

Next, we perform the mechanical stability test by calculating the independent elastic stiffness tensor components. For this 2D lattice with tetragonal symmetry, only C_{11} and C_{12} are nonzero and independent. The calculated elastic constants are $C_{11} = C_{22} = 55.79 \text{ N/m}$ and $C_{12} = 35.89 \text{ N/m}$, which fully meet the Born–Huang criteria.⁴⁶ In this case, the criteria require $C_{11} > |C_{12}|$ and $C_{11} > 0$. Therefore, the TQBQCOF sheet is mechanically stable. To confirm the accuracy of the calculated lattice constants against the choice of the K -point mesh, we repeated the calculations with $4 \times 4 \times 1$ mesh. The resulting elastic constants are $C_{11} = C_{22} = 55.79 \text{ N/m}$ and $C_{12} = 35.84 \text{ N/m}$, which agree very well with the values obtained using $3 \times 3 \times 1$ mesh.

The flexibility or rigidity of a material can be reflected by Young's modulus; a low Young's modulus implies good flexibility for a material. We have calculated the in-plane Young's modulus, $Y(\theta)$, and Poisson's ratio, $\nu(\theta)$, of TQBQCOF by using the method described in SI Section S2.

Due to the high symmetry of the hexagonal lattice, $Y(\theta)$ of TQBQCOF is isotropic with the value of 32.70 N/m along all directions, as shown in Figure 3a. This value is much smaller than that of many other 2D materials, including graphene (1000 N/m),⁴⁷ MoS_2 (330 N/m),⁴⁸ and h-BN (279 N/m),⁴⁹ suggesting that TQBQCOF is flexible and soft. The ratio of transverse strain to longitudinal strain is the definition of Poisson's ratio, reflecting the mechanical response of the system to uniaxial strain. As shown in Figure 3b, the Poisson's ratio curve is almost a circle and the value varies only between 0.65 and 0.73, which further validates the mechanical isotropy of TQBQCOF.

Next, we calculate the 2D TQBQCOF sheet's electronic band structure, as shown in Figure 4a. It can be seen that the 2D TQBQCOF exhibits the semiconducting nature with a direct band gap of 2.70 eV using the HSE06 functional. The corresponding total electronic density of states (TDOS) and the partial electronic density of states (PDOS) are also calculated to analyze the detailed electronic states. Figure 2b shows that N and O atoms are the main contribution of the electronic states near the Fermi level, consistent with the results of the band decomposed charge density distributions (Figure 4c–f).

Because N_2 is a weak Lewis base, it is ideal to create a Lewis acid catalytic site with empty orbitals for the chemical

adsorption of N_2 molecules, which is a vital but challenging step for an effective NRR process. TM-based catalysts possess empty d orbitals that can accept the lone-pair electrons of N_2 and donate d electrons to the antibonding orbitals of N_2 , a process known as π back-donation. Therefore, such “acceptance–donation” of electrons between the TM atoms and N_2 naturally activate the inert $N\equiv N$ triple bond,² where the combination of empty and occupied d orbitals play a key role. Unlike TM atoms, main group non-metal atoms usually lack such a combination. However, the electron-deficient B shows Lewis acid characteristics⁵⁰ and possesses both empty and occupied orbitals, contributing to the chemisorption of N_2 in the NRR process.

The N atoms in the TQBQCOF sheet, all bonded to C atoms, are 2-fold-coordinated, which enables TQBQCOF to incorporate a B atom, as illustrated in Figure 5. Consequently,

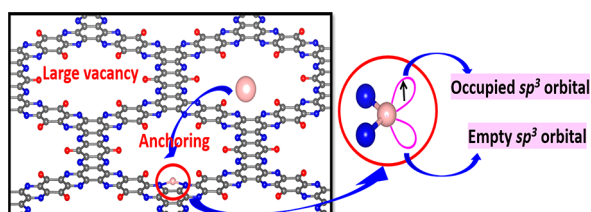


Figure 5. Design concept of B/TQBQCOF catalyst to fix N_2 . The arrow represents single electron spin, and the spindles in violet color stand for the corresponding orbitals. The pink sphere represents B atom.

two newly formed N–B bonds can stabilize the B atom. Meanwhile, the anchored B has one occupied sp^3 orbital and one empty sp^3 orbital, and such a combination can enable the “acceptance–donation” process with N_2 . Additionally, the pores of TQBQCOF are large and regular, which provide sufficient space for the N_2 adsorption and formation of intermediates for the catalytic reduction reaction (see Figure 5). Thus, TQBQCOF could be an ideal substrate to incorporate B and then fix N_2 . The resulting B/TQBQCOF sheet could then be a potential metal-free catalyst to catalyze N_2 .

The optimized structure of B/TQBQCOF is presented in Figure 6a, which continues to be a planar sheet. The binding energy between the B atom and TQBQCOF is 5.19 eV, showing that the TQBQCOF sheet binds B atom strongly and maintains its structure undisturbed after B incorporation.

For an efficient NRR process, capturing of N_2 molecules around the active site initiates the first step of NRR. Hence, we first study the binding energy between N_2 molecules and the B site in B/TQBQCOF via the end-on and side-on adsorption configurations, as illustrated in Figure 6b,c, respectively. The calculation shows that for end-on and side-on adsorption configurations, the adsorption energy between N_2 and B/TQBQCOF is -2.15 and -1.22 eV, respectively. This strong binding strength is attributed to the effective electron–“acceptance–donation” process occurring between the N_2 and B, similar to the TM center in TM-based catalysts.

As for the end-on adsorption, the B atom in B/TQBQCOF bonds with N_2 to form a new chemical bond of length 1.45 Å, while the N–N bond length in the N_2 molecule increases from 1.09 to 1.13 Å. For the side-on pattern, the N_2 and B atoms form two bonds with a bond length of 1.58 Å (see the side view in Figure 6c), whereas the length of the N–N bond

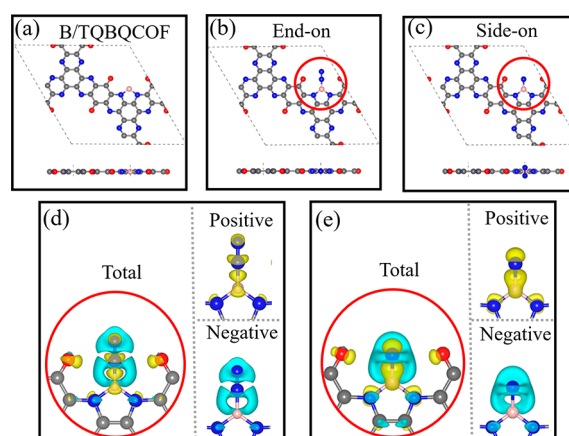


Figure 6. (a–c) Top and side views of B/TQBQCOF, and the adsorption of N_2 on B/TQBQCOF via the end-on and side-on patterns, respectively. Differential charge density of the N_2 adsorbed B/TQBQCOF sheet via (d) end-on and (e) side-on adsorption configurations. The isosurface value is $0.003 e/\text{Å}^3$, and the yellow and cyan represent the distribution of positive and negative charges, respectively.

further increases from 1.09 to 1.19 Å. The enlargement of the N–N bond length in these two cases implies the weakening of the $N\equiv N$ bond, which is beneficial to the later NRR process. Their charge density differences are further calculated and plotted in Figure 6d,e, respectively, showing significant charge transfer between the anchored B atom and N_2 molecule in both the end-on and side-on adsorption patterns. Clearly, two-way charge transfer here is found, and the corresponding charge accumulation and depletion occur to both the N_2 molecule and B atom, which confirms the above-mentioned acceptance–donation process. Therefore, the high binding strength along with the above-mentioned charge transfer phenomenon greatly support facile N_2 activation and reduction on B/TQBQCOF.

We now evaluate the catalytic performance of B/TQBQCOF to reduce N_2 to NH_3 . Three typical mechanisms are considered here, namely, the distal, alternating, and enzymatic catalytic mechanisms, as shown in Figure 7a, which take into account all reaction intermediates. The end-on adsorbed N_2 can be further reduced via pathways of distal and alternating mechanisms. For the pathway of distal mechanism, the proton–electron pair first attacks the distal N to generate a NH_3 molecule and then generates another NH_3 by reacting with the near bonded N. On the contrary, as for the alternating mechanism, the proton–electron pair alternately attacks the two N atoms. The side-on adsorbed N_2 is further hydrogenated through an enzymatic pathway where two N atoms are attacked by proton–electron pairs alternately. Then, the next NH_3 is generated after the releasing of the first NH_3 .

To study the change of free energy in the NRR process, we calculate the vibrational frequencies, zero-point energies, and entropies of intermediates for the side-on and end-on adsorption patterns, respectively. These results are summarized in Table S3. The corresponding free energy diagrams for the above three pathways are plotted in Figure 7b–d. For end-on adsorption, the N_2 adsorbed on B/TQBQCOF can be further reduced with an energy uphill of 0.64 eV, while that is only 0.07 eV for the side-on adsorption, because of the strong binding strength between N_2 and B/TQBQCOF. For

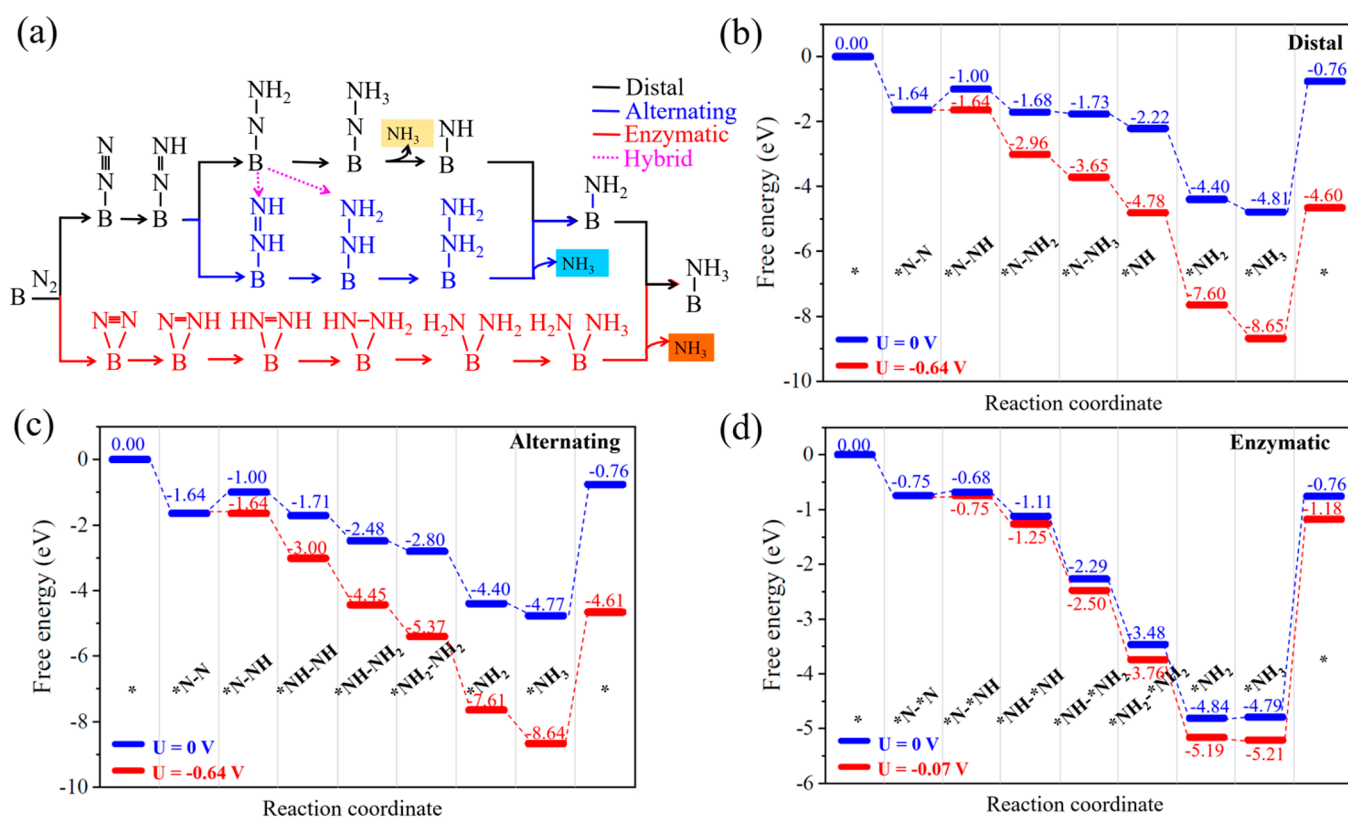


Figure 7. (a) Schematic illustration of three main mechanisms for the N₂ reduction. Free energy diagrams of the three mechanisms discussed in text for N₂ reduction on B/TQBQCOF through the (b) distal, (c) alternating, and (d) enzymatic mechanisms at different applied potentials. The purple dotted line presents the hybrid mechanism.

subsequent basic reaction steps via the distal pathway, they are all exothermic and generate NH₃ spontaneously. The corresponding free energy downhill for the generation of the first and second NH₃ is -0.49 and -0.41 eV, respectively. The only one free energy uphill in the distal pathway is the $*NN \rightarrow *NNH$, which is the potential-determining step with an onset potential of 0.64 V for this NRR process (see Figure 7b). As for the alternating mechanism, the process of $*N-N$ hydrogenated into $*N-NH$ is also the only one free energy uphill of 0.64 eV, resulting in an onset potential of 0.64 V (Figure 7c). This is the same as that of the distal pathway. In the case of the enzymatic mechanism, except for the step $*N-*N + H^+ + e^- = *N-*NH$, the subsequent steps are all exothermic as presented in Figure 7d.

Following a recent study of hybrid mechanism for N₂ reduction,⁵¹ we also consider this in B/TQBQCOF, as shown in Figure 7a. For the pathway of $*N-NH_2 \rightarrow *NH-NH$, the free energy change is only 0.001 eV, while for the pathway of $*N-NH_2 \rightarrow *NH-NH_2$, the free energy change is -4.21 eV, implying that this is a spontaneous process. However, for hybrid steps, the free energy change of potential-determining step ($*NN \rightarrow *NNH$) is 0.64 eV, which is much larger than the value of 0.07 eV in enzymatic pathway. Therefore, the hybrid mechanism is energetically less favorable than the enzymatic mechanism. Obviously, there are rich N sites in TQBQCOF, which can easily adsorb H species, causing the competition between the NH₃ and H₂ release.⁵² Hence, following the procedure in the process of NRR, we investigate the free energy change in hydrogen evolution reaction (HER) for H species. The calculated results are plotted in Figure S4. The rich N-sites can easily adsorb H

species, and the corresponding free energy change in HER is -0.62 eV, while in the NRR process, the corresponding value change is -1.64 , -1.64 , and -0.75 eV for the distal, alternating, and enzymatic mechanisms, respectively, suggesting the priority for N₂ adsorption, thus leading to a good selectivity of NH₃ generation. Therefore, one can see that the basic process in the whole reaction requires an energy injection of 0.07 eV, resulting in a low onset potential. This is the lowest value among all other metal or metal-free NRR catalysts reported so far. Hence, the B/TQBQCOF sheet is a potential metal-free catalyst for NRR with lowest onset potential.

Generally speaking, the catalytic site adsorbing N₂ successfully is a decisive step for the whole NRR process. On one hand, it is difficult for catalyst to adsorb N₂ because N₂ is an extremely inert molecule with a stable N≡N bond. On the other hand, the N₂ adsorption process on the catalyst does not involve the transfer of electron–proton pairs, so the energy barrier for this process cannot be controlled and adjusted by an external voltage. Therefore, it is important to investigate the N₂ adsorption process. In order to study the transition state of N₂ adsorbed on the B site through the above-mentioned configurations, we first construct the intermediate state structures by the structure-dependent image-dependent pair potential (IDPP) method.⁵³ Next, we apply the climbing image nudged elastic band (CI-NEB) method⁵⁴ to calculate the ground state energy of each intermediate state and determine the transition state (TS), which is the configuration with the highest energy barrier of the intermediate state. The reason why we apply the IDPP method to interpolate the distance between atoms rather than simply linearly interpolate the atomic coordinates is that the IDPP method retains a more

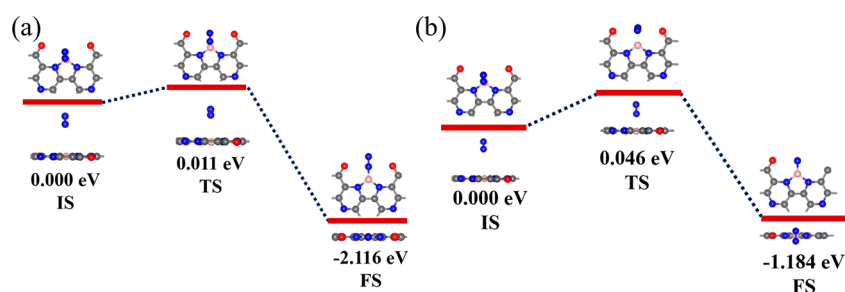


Figure 8. Schematic energy profile of N_2 with (a) end-on and (b) side-on adsorption configurations.

integral structure of the N_2 rotation and avoids the generation of unreasonable structures.

Therefore, on the basis of the IDPP method, we generate a variety of intermediate structures between the initial (IS) and the final state (FS). The transition state energy barriers for end-on and side-on adsorptions are calculated and displayed in Figure 8, showing that the transition state energy barrier of the end-on adsorption is 0.011 eV, while that is 0.046 eV for the side-on adsorption. One can see that whether N_2 is adsorbed to the B catalytic site via the end-on or side-on adsorption, the corresponding transition state energy barrier for this process is very low, indicating that N_2 can be easily adsorbed on the B site. The intermediate product $*NN$ or $*N-N$ creates a prerequisite for the further catalytic reduction of N_2 .

In summary, we have proposed a 2D TQBQCOF sheet that is exfoliated from the synthesized covalent organic frameworks consisting of multiple carbonyls and pyrazine groups. By employing first-principles calculations combined with the CHE model, we have systematically studied the geometric structures and electronic and mechanical properties of TQBQCOF as well as the N_2 fixation on the B/TQBQCOF sheet. The following conclusions can be drawn: (1) TQBQCOF is not only mechanically and dynamically stable but also can withstand temperatures up to 1200 K. (2) It possesses a hexagonal planar structure with the lattice group symmetry of $P4/m3m$, and has almost isotropic mechanical properties with a low isotropic Young's modulus of 32.70 N/m, lower than that of most 2D materials. (3) The TQBQCOF sheet can bind B atom strongly with a binding energy of 5.19 eV, forming a stable planar sheet, B/TQBQCOF, which can further bind N_2 at the B site with the adsorption energies of -2.15 and -1.22 eV for the end-on and side-on adsorption configurations, respectively. (4) The rate-determining steps of the three catalytic pathways for N_2 reduction on B/TQBQCOF are $*N-N \rightarrow *N-NH$. For the entire catalytic pathway for both the distal and alternating mechanisms, the required overpotential for N_2 reduction is 0.64 V, while for the enzymatic catalytic mechanism, only a very low voltage of 0.07 V is needed to achieve the green conversion. To the best of our knowledge, this is a catalyst that requires the lowest applied voltage among all of the catalysts for N_2 reduction reported so far. Our study shows that B/TQBQCOF is a promising metal-free catalyst for effective reduction of N_2 to NH_3 .

■ ASSOCIATED CONTENT

SI Supporting Information

The Supporting Information is available free of charge at <https://pubs.acs.org/doi/10.1021/acs.jpcllett.1c02502>.

Additional data and figures, including the binding energy and free energy (ΔG); Young's modulus and Poisson's

ratio; Wyckoff positions in TQBQCOF; geometrical parameters of TQBQCOF; calculated vibrational frequencies, zero-point energies, and entropy; intermediate structures for NRR; free energy diagram of HER; and POSCAR of TQBQCOF sheet (PDF)

■ AUTHOR INFORMATION

Corresponding Authors

Qian Wang – Center for Applied Physics and Technology, College of Engineering, Peking University, Beijing 100871, China; School of Materials Science and Engineering, BKL-MEMD, Peking University, Beijing 100871, China; orcid.org/0000-0002-9766-4617; Email: qianwang2@pku.edu.cn

Puru Jena – Department of Physics, Virginia Commonwealth University, Richmond, Virginia 23284, United States; orcid.org/0000-0002-2316-859X; Email: pjena@vcu.edu

Authors

Wenyang Zhou – Center for Applied Physics and Technology, College of Engineering, Peking University, Beijing 100871, China; School of Materials Science and Engineering, BKL-MEMD, Peking University, Beijing 100871, China; Navigation and Control Technology Institute, NORINCO GROUP, Beijing 100089, China

Haoming Shen – School of Materials Science and Engineering, BKL-MEMD, Peking University, Beijing 100871, China; Center for Applied Physics and Technology, College of Engineering, Peking University, Beijing 100871, China; orcid.org/0000-0001-7715-9739

Huanhuan Xie – School of Materials Science and Engineering, BKL-MEMD, Peking University, Beijing 100871, China; Center for Applied Physics and Technology, College of Engineering, Peking University, Beijing 100871, China; orcid.org/0000-0002-3292-9039

Yiheng Shen – Center for Applied Physics and Technology, College of Engineering, Peking University, Beijing 100871, China; School of Materials Science and Engineering, BKL-MEMD, Peking University, Beijing 100871, China

Wei Kang – Center for Applied Physics and Technology, College of Engineering, Peking University, Beijing 100871, China

Yoshiyuki Kawazoe – New Industry Creation Hatchery Center, Tohoku University, Sendai 980-8577, Japan; Department of Physics and Nanotechnology, SRM Institute of Science and Technology, Kattankulathur 603203 Tamil Nadu, India; School of Physics, Suranaree University of Technology, Nakhon Ratchasima 30000, Thailand

Complete contact information is available at:

<https://pubs.acs.org/10.1021/acs.jpcllett.1c02502>

Notes

The authors declare no competing financial interest.

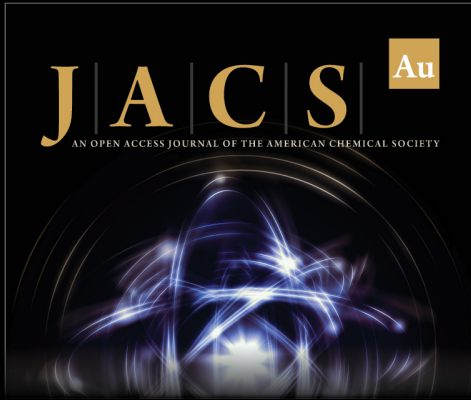
ACKNOWLEDGMENTS

This work is partially supported by grants from the National Key Research and Development Program of the Ministry of Science and Technology of China (2017YFA0205003) and the National Natural Science Foundation of China (NSFC-11974028 and NSFC-21773004) and is supported by the High-Performance Computing Platform of Peking University, China. P.J. acknowledges partial support by the U.S. Department of Energy (DOE), Office of Basic Energy Sciences, Division of Material Sciences and Engineering under Award No. DE-FG02-96ER45579. We thank the crew of the Center for Computational Materials Science, the Institute for Materials Research, Tohoku University (Japan), for their continuous support of the MASAMUNE-IMR supercomputing facility. W.Z. acknowledges the China Scholarship Council (CSC) for sponsoring his visit to Virginia Commonwealth University (VCU).

REFERENCES

- (1) Zhao, J.; Chen, Z. Single Mo Atom Supported on Defective Boron Nitride Monolayer as an Efficient Electrocatalyst for Nitrogen Fixation: A Computational Study. *J. Am. Chem. Soc.* **2017**, *139* (36), 12480–12487.
- (2) Légaré, M.-A.; Bélanger-Chabot, G.; Dewhurst, R. D.; Welz, E.; Krummenacher, I.; Engels, B.; Braunschweig, H. Nitrogen fixation and reduction on boron. *Science* **2018**, *359* (6378), 896.
- (3) Foster, S. L.; Bakovic, S. I. P.; Duda, R. D.; Maheshwari, S.; Milton, R. D.; Minter, S. D.; Janik, M. J.; Renner, J. N.; Greenlee, L. F. Catalysts for nitrogen reduction to ammonia. *Nat. Catal.* **2018**, *1* (7), 490–500.
- (4) Suryanto, B. H. R.; Du, H.-L.; Wang, D.; Chen, J.; Simonov, A. N.; MacFarlane, D. R. Challenges and prospects in the catalysis of electroreduction of nitrogen to ammonia. *Nat. Catal.* **2019**, *2* (4), 290–296.
- (5) Chen, J. G.; Crooks, R. M.; Seefeldt, L. C.; Bren, K. L.; Bullock, R. M.; Darensbourg, M. Y.; Holland, P. L.; Hoffman, B.; Janik, M. J.; Jones, A. K.; Kanatzidis, M. G.; King, P.; Lancaster, K. M.; Lyman, S. V.; Pfomm, P.; Schneider, W. F.; Schrock, R. R. Beyond fossil fuel-driven nitrogen transformations. *Science* **2018**, *360* (6391), eaar6611.
- (6) Jin, H.; Guo, C.; Liu, X.; Liu, J.; Vasileff, A.; Jiao, Y.; Zheng, Y.; Qiao, S.-Z. Emerging Two-Dimensional Nanomaterials for Electrocatalysis. *Chem. Rev.* **2018**, *118* (13), 6337–6408.
- (7) Erisman, J. W.; Sutton, M. A.; Galloway, J.; Klimont, Z.; Winiwarter, W. How a century of ammonia synthesis changed the world. *Nat. Geosci.* **2008**, *1* (10), 636–639.
- (8) Kitano, M.; Kanbara, S.; Inoue, Y.; Kuganathan, N.; Sushko, P. V.; Yokoyama, T.; Hara, M.; Hosono, H. Electride support boosts nitrogen dissociation over ruthenium catalyst and shifts the bottleneck in ammonia synthesis. *Nat. Commun.* **2015**, *6*, 6731.
- (9) Zhang, L.; Ji, X.; Ren, X.; Ma, Y.; Shi, X.; Tian, Z.; Asiri, A. M.; Chen, L.; Tang, B.; Sun, X. Electrochemical Ammonia Synthesis via Nitrogen Reduction Reaction on a MoS₂ Catalyst: Theoretical and Experimental Studies. *Adv. Mater.* **2018**, *30* (28), 1800191.
- (10) Shi, M.-M.; Bao, D.; Wulan, B.-R.; Li, Y.-H.; Zhang, Y.-F.; Yan, J.-M.; Jiang, Q. Au Sub-Nanoclusters on TiO₂ toward Highly Efficient and Selective Electrocatalyst for N₂ Conversion to NH₃ at Ambient Conditions. *Adv. Mater.* **2017**, *29* (17), 1606550.
- (11) Li, S.-J.; Bao, D.; Shi, M.-M.; Wulan, B.-R.; Yan, J.-M.; Jiang, Q. Amorphizing of Au Nanoparticles by CeO_x-RGO Hybrid Support towards Highly Efficient Electrocatalyst for N₂ Reduction under Ambient Conditions. *Adv. Mater.* **2017**, *29* (33), 1700001.
- (12) Seh, Z. W.; Kibsgaard, J.; Dickens, C. F.; Chorkendorff, I. B.; Norskov, J. K.; Jaramillo, T. F. Combining theory and experiment in electrocatalysis: Insights into materials design. *Science* **2017**, *355* (6321), eaad4998.
- (13) Wang, M.; Liu, S.; Qian, T.; Liu, J.; Zhou, J.; Ji, H.; Xiong, J.; Zhong, J.; Yan, C. Over 56.55% Faradaic efficiency of ambient ammonia synthesis enabled by positively shifting the reaction potential. *Nat. Commun.* **2019**, *10* (1), 341.
- (14) Geng, Z.; Liu, Y.; Kong, X.; Li, P.; Li, K.; Liu, Z.; Du, J.; Shu, M.; Si, R.; Zeng, J. Achieving a Record-High Yield Rate of 120.9 for N₂ Electrochemical Reduction over Ru Single-Atom Catalysts. *Adv. Mater.* **2018**, *30* (40), 1803498.
- (15) Su, J.; Zhao, H.; Fu, W.; Tian, W.; Yang, X.; Zhang, H.; Ling, F.; Wang, Y. Fine rhodium phosphides nanoparticles embedded in N, P dual-doped carbon film: New efficient electrocatalysts for ambient nitrogen fixation. *Appl. Catal., B* **2020**, *265*, 118589.
- (16) Shi, M.-M.; Bao, D.; Li, S.-J.; Wulan, B.-R.; Yan, J.-M.; Jiang, Q. Anchoring PdCu Amorphous Nanocluster on Graphene for Electrochemical Reduction of N₂ to NH₃ under Ambient Conditions in Aqueous Solution. *Adv. Energy Mater.* **2018**, *8* (21), 1800124.
- (17) Bao, D.; Zhang, Q.; Meng, F.-L.; Zhong, H.-X.; Shi, M.-M.; Zhang, Y.; Yan, J.-M.; Jiang, Q.; Zhang, X.-B. Electrochemical Reduction of N₂ under Ambient Conditions for Artificial N₂ Fixation and Renewable Energy Storage Using N₂/NH₃ Cycle. *Adv. Mater.* **2017**, *29* (3), 1604799.
- (18) Lan, R.; Irvine, J. T.; Tao, S. J. S. r. Synthesis of ammonia directly from air and water at ambient temperature and pressure. *Sci. Rep.* **2013**, *3* (1), 1145.
- (19) Cao, N.; Chen, Z.; Zang, K.; Xu, J.; Zhong, J.; Luo, J.; Xu, X.; Zheng, G. J. N. c. Doping strain induced bi-Ti³⁺ pairs for efficient N₂ activation and electrocatalytic fixation. *Nat. Commun.* **2019**, *10* (1), 2877.
- (20) Sekiguchi, Y.; Arashiba, K.; Tanaka, H.; Eizawa, A.; Nakajima, K.; Yoshizawa, K.; Nishibayashi, Y. Catalytic Reduction of Molecular Dinitrogen to Ammonia and Hydrazine Using Vanadium Complexes. *Angew. Chem., Int. Ed.* **2018**, *57* (29), 9064–9068.
- (21) Nash, J.; Yang, X.; Anibal, J.; Dunwell, M.; Yao, S.; Attenkofer, K.; Chen, J. G.; Yan, Y.; Xu, B. Elucidation of the Active Phase and Deactivation Mechanisms of Chromium Nitride in the Electrochemical Nitrogen Reduction Reaction. *J. Phys. Chem. C* **2019**, *123* (39), 23967–23975.
- (22) Ma, D.; Zeng, Z.; Liu, L.; Huang, X.; Jia, Y. Computational evaluation of electrocatalytic nitrogen reduction on TM single-, double-, and triple-atom catalysts (TM = Mn, Fe, Co, Ni) based on graphdiyne monolayers. *J. Phys. Chem. C* **2019**, *123* (31), 19066–19076.
- (23) He, C.; Wu, Z.-Y.; Zhao, L.; Ming, M.; Zhang, Y.; Yi, Y.; Hu, J.-S. J. A. C. Identification of FeN₄ as an efficient active site for electrochemical N₂ reduction. *ACS Catal.* **2019**, *9* (8), 7311–7317.
- (24) Liu, Y.; Xu, Q.; Fan, X.; Quan, X.; Su, Y.; Chen, S.; Yu, H.; Cai, Z. Electrochemical reduction of N₂ to ammonia on Co single atom embedded N-doped porous carbon under ambient conditions. *J. Mater. Chem. A* **2019**, *7* (46), 26358–26363.
- (25) Yuan, M.; Zhang, H.; Gao, D.; He, H.; Sun, Y.; Lu, P.; Dipazir, S.; Li, Q.; Zhou, L.; Li, S.; et al. Support effect boosting the electrocatalytic N₂ reduction activity of Ni₂P/N,P-codoped carbon nanosheet hybrids. *J. Mater. Chem. A* **2020**, *8* (5), 2691–2700.
- (26) Han, J.; Liu, Z.; Ma, Y.; Cui, G.; Xie, F.; Wang, F.; Wu, Y.; Gao, S.; Xu, Y.; Sun, X. J. N. E. Ambient N₂ fixation to NH₃ at ambient conditions: Using Nb₂O₅ nanofiber as a high-performance electrocatalyst. *Nano Energy* **2018**, *52*, 264–270.
- (27) Zhang, J.; Tian, X.; Liu, M.; Guo, H.; Zhou, J.; Fang, Q.; Liu, Z.; Wu, Q.; Lou, J. Cobalt-modulated molybdenum-dinitrogen interaction in MoS₂ for catalyzing ammonia synthesis. *J. Am. Chem. Soc.* **2019**, *141* (49), 19269–19275.
- (28) Jin, H.; Li, L.; Liu, X.; Tang, C.; Xu, W.; Chen, S.; Song, L.; Zheng, Y.; Qiao, S. Z. J. A. M. Nitrogen vacancies on 2D layered W₂N₃: a stable and efficient active site for nitrogen reduction reaction. *Adv. Mater.* **2019**, *31* (32), 1902709.

- (29) Hao, Y.-C.; Guo, Y.; Chen, L.-W.; Shu, M.; Wang, X.-Y.; Bu, T.-A.; Gao, W.-Y.; Zhang, N.; Su, X.; Feng, X.; Zhou, J.-W.; Wang, B.; Hu, C.-W.; Yin, A.-X.; Si, R.; Zhang, Y.-W.; Yan, C.-H. Promoting nitrogen electroreduction to ammonia with bismuth nanocrystals and potassium cations in water. *Nat. Catal.* **2019**, *2* (5), 448–456.
- (30) Li, L.; Tang, C.; Xia, B.; Jin, H.; Zheng, Y.; Qiao, S.-Z. Two-Dimensional Mosaic Bismuth Nanosheets for Highly Selective Ambient Electrocatalytic Nitrogen Reduction. *ACS Catal.* **2019**, *9* (4), 2902–2908.
- (31) Li, P.; Fu, W.; Zhuang, P.; Cao, Y.; Tang, C.; Watson, A. B.; Dong, P.; Shen, J.; Ye, M. Amorphous Sn/Crystalline SnS₂ Nanosheets via In Situ Electrochemical Reduction Methodology for Highly Efficient Ambient N₂ Fixation. *Small* **2019**, *15* (40), 1902535.
- (32) Chu, K.; Liu, Y.-p.; Li, Y.-b.; Wang, J.; Zhang, H. Electronically Coupled SnO₂ Quantum Dots and Graphene for Efficient Nitrogen Reduction Reaction. *ACS Appl. Mater. Interfaces* **2019**, *11* (35), 31806–31815.
- (33) Qu, L.; Liu, Y.; Baek, J.-B.; Dai, L. Nitrogen-Doped Graphene as Efficient Metal-Free Electrocatalyst for Oxygen Reduction in Fuel Cells. *ACS Nano* **2010**, *4* (3), 1321–1326.
- (34) Welch, G. C.; Juan, R. R. S.; Masuda, J. D.; Stephan, D. W. Reversible, metal-free hydrogen activation. *Science* **2006**, *314* (5802), 1124–1126.
- (35) Yang, S.; Feng, X.; Wang, X.; Muellen, K. Graphene-Based Carbon Nitride Nanosheets as Efficient Metal-Free Electrocatalysts for Oxygen Reduction Reactions. *Angew. Chem., Int. Ed.* **2011**, *50* (23), 5339–5343.
- (36) Shi, R.; Liu, L.; Lu, Y.; Wang, C.; Li, Y.; Li, L.; Yan, Z.; Chen, J. Nitrogen-rich covalent organic frameworks with multiple carbonyls for high-performance sodium batteries. *Nat. Commun.* **2020**, *11* (1), 178.
- (37) Zhou, W.; Shen, H.; Wang, Q.; Onoe, J.; Kawazoe, Y.; Jena, P. N-doped peanut-shaped carbon nanotubes for efficient CO₂ electrocatalytic reduction. *Carbon* **2019**, *152*, 241–246.
- (38) Blöchl, P. E. Projector augmented-wave method. *Phys. Rev. B: Condens. Matter Mater. Phys.* **1994**, *50* (24), 17953.
- (39) Kresse, G.; Furthmüller, J. Efficient iterative schemes for ab initio total-energy calculations using a plane-wave basis set. *Phys. Rev. B: Condens. Matter Mater. Phys.* **1996**, *54* (16), 11169.
- (40) Perdew, J. P.; Burke, K.; Ernzerhof, M. J. P. R. L. Generalized gradient approximation made simple. *Phys. Rev. Lett.* **1996**, *77* (18), 3865.
- (41) Monkhorst, H. J.; Pack, J. D. Special points for Brillouin-zone integrations. *Phys. Rev. B* **1976**, *13* (12), 5188–5192.
- (42) Allen, M. J.; Tung, V. C.; Kaner, R. B. Honeycomb Carbon: A Review of Graphene. *Chem. Rev.* **2010**, *110* (1), 132–145.
- (43) Tan, C.; Cao, X.; Wu, X.-J.; He, Q.; Yang, J.; Zhang, X.; Chen, J.; Zhao, W.; Han, S.; Nam, G.-H.; Sindoro, M.; Zhang, H. Recent Advances in Ultrathin Two-Dimensional Nanomaterials. *Chem. Rev.* **2017**, *117* (9), 6225–6331.
- (44) Geick, R.; Perry, C. H.; Rupprecht, G. Normal Modes in Hexagonal Boron Nitride. *Phys. Rev.* **1966**, *146* (2), 543–547.
- (45) Nosé, S. A unified formulation of the constant temperature molecular dynamics methods. *J. Chem. Phys.* **1984**, *81* (1), 511–519.
- (46) Born, M.; Huang, K. *Dynamical theory of crystal lattices*; Clarendon Press, 1954.
- (47) Lee, C.; Wei, X.; Kysar, J. W.; Hone, J. Measurement of the Elastic Properties and Intrinsic Strength of Monolayer Graphene. *Science* **2008**, *321* (5887), 385.
- (48) Castellanos-Gomez, A.; Poot, M.; Steele, G. A.; Van Der Zant, H. S.; Agraït, N.; Rubio-Bollinger, G. J. A. m. Elastic properties of freely suspended MoS₂ nanosheets. *Adv. Mater.* **2012**, *24* (6), 772–775.
- (49) Peng, Q.; Ji, W.; De, S. Mechanical properties of the hexagonal boron nitride monolayer: Ab initio study. *Comput. Mater. Sci.* **2012**, *56*, 11–17.
- (50) Yu, X.; Han, P.; Wei, Z.; Huang, L.; Gu, Z.; Peng, S.; Ma, J.; Zheng, G. Boron-Doped Graphene for Electrocatalytic N₂ Reduction. *Joule* **2018**, *2* (8), 1610–1622.
- (51) Anderson, J. S.; Cutsail, G. E., III; Rittle, J.; Connor, B. A.; Gunderson, W. A.; Zhang, L.; Hoffman, B. M.; Peters, J. C. Characterization of an Fe≡N–NH₂ Intermediate Relevant to Catalytic N₂ Reduction to NH₃. *J. Am. Chem. Soc.* **2015**, *137* (24), 7803–7809.
- (52) Ma, D.; Wang, Y.; Liu, L.; Jia, Y. J. P. C. C. P. *Phys. Chem. Chem. Phys.* **2021**, *23* (6), 4018–4029.
- (53) Smidstrup, S.; Pedersen, A.; Stokbro, K.; Jónsson, H. Improved initial guess for minimum energy path calculations. *J. Chem. Phys.* **2014**, *140* (21), 214106.
- (54) Henkelman, G.; Uberuaga, B. P.; Jónsson, H. A climbing image nudged elastic band method for finding saddle points and minimum energy paths. *J. Chem. Phys.* **2000**, *113* (22), 9901–9904.



JACS Au
AN OPEN ACCESS JOURNAL OF THE AMERICAN CHEMICAL SOCIETY

Editor-in-Chief
Prof. Christopher W. Jones
Georgia Institute of Technology, USA

Open for Submissions 

pubs.acs.org/jacsau  ACS Publications
Most Trusted. Most Cited. Most Read.